Synthesis and characterization of $La_2Mo_2O_9$ obtained from freeze-dried precursors

D. Marrero-López,[a] J.C. Ruiz-Morales,[a] P. Núñez,[a,*] J.C.C. Abrantes,[b] and J.R. Frade[c]

[a] Departamento de Química Inorgánica, Universidad de La Laguna, Astrofísico Francisco Sanchez, sn E-38206 La Laguna, Tenerife, Spain
[b] ESTG, Instituto Politécnico de Viana do Castelo, 4900 Viana do Castelo, Portugal
[c] Department of Engenharia Cerâmica e do Vidro, CICECO, Universidade de Aveiro, 3810-193 Aveiro, Portugal

Abstract

$La_2Mo_2O_9$ ceramics have been prepared from freeze-dried precursors and their properties compared to those of lantanum molybdate obtained by conventional solid state (SS) reaction. All materials have been characterized by X-ray diffraction, scanning electron microscopy and thermal analysis (TGA/DTA/DSC and dilatometry) to characterize the phase formation and phase transition. When the freeze-dried method was applied, the synthesis temperature required to obtain dense samples was much lower than that for powders obtained by SS reaction. The morphology and structure of the oxide particle are significantly dependent on the synthesis method. The grain size is smaller, whereas the density of sintered pellets is higher for the freeze-dried precursor powder when compared with the SS reaction method. Impedance spectroscopy was used to measure the electrical conductivity of $La_2Mo_2O_9$ from 548 to 1123 K, in air, and to characterize the blocking effects of grain boundaries.

1. Introduction

Oxide ion conductors have been increasingly studied for many years because of their potential applications in many devices with high economical interest, such as components of fuel cells, oxygen sensors, dense ceramic for oxygen separation membranes, oxygen pumps and oxygen-permeable membrane catalysts [1–4]. New fields of applications have appeared in this research area because new phases allow significant reduction of operating temperature. In addition to the intrinsic basic properties, the role of microstructure has been emphasized, leading to the development of new routes for solid synthesis and new techniques for ceramic manufacturing [5,6].

Most important oxide ion conductors belong to four distinct structural groups, [7–10] which include the doped perovskite-type ABO_3 (doped $LaGaO_3$) [11–13], fluorite-type (stabilized zirconia [14], ceria [15–17], δ-Bi_2O_3 [18]), Aurivillius-type phases BIMEVOX [19,20]

and pyrochlores [21,22]. In addition, a new kind of oxide ion conductor [23–28] has been reported recently, $La_2Mo_2O_9$, which exhibits good ionic conductivity at low temperature and has a crystal structure which differs from previous fast oxide ion conductors.

For traditional oxide ion conductors, such as AO_2 fluorite-type anionic vacancies are generated by substitution of tetravalent cations by tri- or divalent cations, thus recovering charge neutrality. Similar charge compensation is found for doped ABO_3 perovskite materials with partial substitution of A and/or B cations by lower-valence cations. Doping with aliovalent species is thus essential to attain high concentrations of effective charge carriers (oxygen vacancies), and high ionic conductivity in these materials. On the contrary, the structure of $La_2Mo_2O_9$ possesses a significant fraction of vacant intrinsic oxygen sites, which allows accommodation of oxygen excess in the structure [23,24]. The high conductivity of these materials has also been related to migrations of oxygen ions via vacant sites.

The conducting properties of $La_2Mo_2O_9$ were also interpreted by the Lone Pair Substitution concept [29].

*Corresponding author. Fax: +34-922318461.
E-mail address: pnunez@ull.es (P. Núñez).

The crystal structure of β-$La_2Mo_2O_9$ resembles that of β-$SnWO_4$, which was reformulated as $Sn_2W_2O_8L_2$, where L is the lone pair of Sn^{2+}. In $La_2Mo_2O_9$, molybdenum replaces tungsten and Sn^{2+} is substituted by La^{3+} (without lone pair). Thus, the lone pair site either remains as a vacant site or can be occupied by oxide anions due to the higher valence of La^{3+}. The structural formula of lanthanum molybdate was thus rewritten as $La_2Mo_2O_{8+1}\square$ (where $\square$ is a vacancy). The extra oxide anions can migrate through the vacancies justifying its high conductivity.

This material undergoes a structural transition (around 843 K). The high-temperature polymorph β-$La_2Mo_2O_9$ is cubic ($P2_13$ space group) and the low-temperature polymorph α-$La_2Mo_2O_9$ has been considered as a $2 \times 3 \times 4$ superstructure of the cubic form with a monoclinic distortion [24]. However, a definitive structural determination for the α form is lacking. Several partial substitutions have been tested in $La_2Mo_2O_9$ by replacing both La and Mo for equivalent cations. La has been substituted by Sr, Ba, K, Bi [26], Ca, [27] and Mo for Re, Cr, V [26], W [28], Nb, Ta [30]. It seems that some of these substitutions may stabilize the β-cubic structure down to room temperature. However, those additives often lower the ionic conductivity.

In the current investigation, we report the preparation of $La_2Mo_2O_9$ ceramics from different powders prepared by a freeze-drying method (FD), and by a conventional solid state reaction (SS). The freeze-dried precursor method yields crystalline single phase precursors at lower temperatures, which are suitable to reassess the phase transition in these materials. In addition, these very fine crystalline precursors can be used to obtain nearly fully dense samples, without excessive firing temperatures. Preparation of dense $La_2Mo_2O_9$ ceramics has not been reported in Literature. By extending the sintering time and/or temperature one may be able to adjust the microstructural features, and to optimize corresponding grain boundary effects on transport properties and/or thermomechanical performance.

2. Experimental

2.1. Synthesis

Powders of $La_2Mo_2O_9$ were prepared by conventional SS reaction of La_2O_3 (99.9% Aldrich) and MoO_3 (99.9% Merck). Lanthanum oxide was previously calcined at 1273 K, during 2 h, to remove water and organics, to ensure a proper stoichiometric ratio. Lanthanum and molybdenum oxides were well mixed in stoichiometric proportions and fired in an alumina crucible at 773 K, for 5 h, then finely grounded and calcined again at 1223 K for 5 h.

The freeze-dried precursors were prepared from solutions obtained by dissolving La_2O_3 with diluted nitric acid, and dissolving MoO_3 with diluted ammonia, which was heated to remove the ammonia excess leading to a final pH near 7. These two solutions were mixed in stoichiometric amounts. A typical 100 mL resulting solution contains 1.792 g (0.011 mol of La^{3+}) of La_2O_3 and 1.583 g of MoO_3. Droplets of this solution were flash frozen by projecting into liquid nitrogen and then FD at pressure of 1–10 Pa in a Heto Lyolab 3000 freeze dryer, during 2 days. In this way, about 3 g of dried solid precursors were obtained as amorphous loose powders. The precursor powder was heated in an alumina crucible at 5 K min^{-1} to 673 K for 5 h and finally cooled down slowly to room temperature.

2.2. X-ray diffraction

Powder X-ray diffraction patterns were obtained with a Philips X'Pert diffractometer using CuKα and graphite secondary beta monochromator. The 2θ range was 5–80° with a step of 0.02° and step time of 2 s. High-temperature measurements were carried out using an Anton Paar TTK 450 Camera, under vacuum (5.5×10^{-2} Pa) and air conditions at different temperatures up to 1023 K. The heating rate was 5 K min^{-1} and the sample was left during 10 min at each temperature before the measurement in order to stabilize the equipment and sample. The FULLPROF program [31] was used for whole pattern fitting by a least-squares method, assisted by WinPlotr for visualization [32].

Fig. 1 shows the X-ray diffractograms of freeze-dried $La_2Mo_2O_9$ powders after heating at different temperatures between 673 and 1223 K. Though a single phase $La_2Mo_2O_9$ is already obtained after firing at 673 K for only 5 h, and above 873 K the X-rays patterns do not
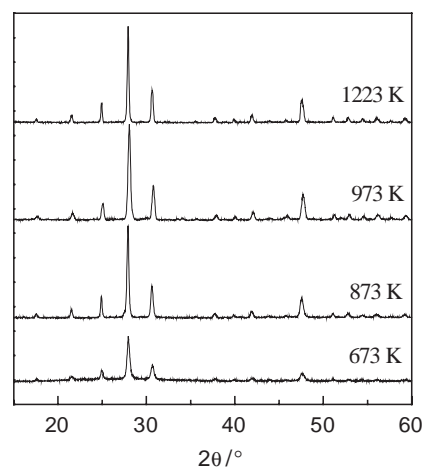

Fig. 1. XRD pattern of $La_2Mo_2O_9$ prepared from freeze-dried precursor and calcined during 5 h at different temperatures: (a) 673 K; (b) 873 K; (c) 973 K, and (d) 1223 K.

show notable changes in the crystallinity, most samples were calcined between 973 and 1223 K to ensure good crystallinity for XRD measurements. The crystalline size was evaluated from Scherrer's equation as 15 nm for FD sample fired at 673 K, increasing to 50 nm for samples fired at 1223 K.

In the case of samples prepared by SS reaction, a calcining temperature of 1223 K was necessary to get a single phase.

2.3. Thermal analysis

Simultaneous Thermogravimetric Analysis (TGA) and Differential Thermal Analysis (DTA) were performed on a Perkin Elmer mod. Pyris Diamond TG/DTA. The temperature was varied from room temperature up to 1173 K at a heating rate of 10 K min^{-1} in a nitrogen flux (20 cm^3 min^{-1}). No mass loss was observed in the temperature range by TGA. Differential Scanning Calorimetry (DSC) Analysis was recorded on a Perkin Elmer mod. Pyris Diamond DSC.

A TMA (Perkin Elmer, mod. Pyris Diamond) equipment was used to evaluate the sinterability of samples prepared from FD and SS, to identify the temperature at which the shrinkage rate reaches a maximum, and to determine the thermal expansion of sintered samples. The results shown in Fig. 2 clearly demonstrate that the freeze-dried precursor reduces the temperature at which the shrinkage rate peak is reached. This is an advantage concerning the preparation of dense samples, at relatively lower temperatures, and to be able to prepare samples with fine grain sizes often contributes to improved thermomechanical performance of the samples.
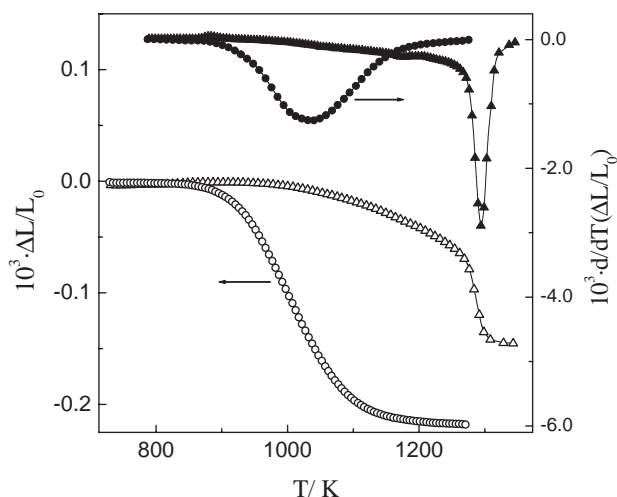
2.4. Microstructural characterization

The morphology of both powders and sintered pellets was observed using a Scanning Electron Microscope (Jeol Ltd., JSM-6300) operating at an accelerating voltage of 30 kV. All preparations were covered with a thin film of gold for better image definition. The microstructures of sintered pellets are significantly dependent on the powder synthesis and sintering conditions. The SEM images shown in Fig. 3 correspond to sintered pellets of $La_2Mo_2O_9$ obtained by
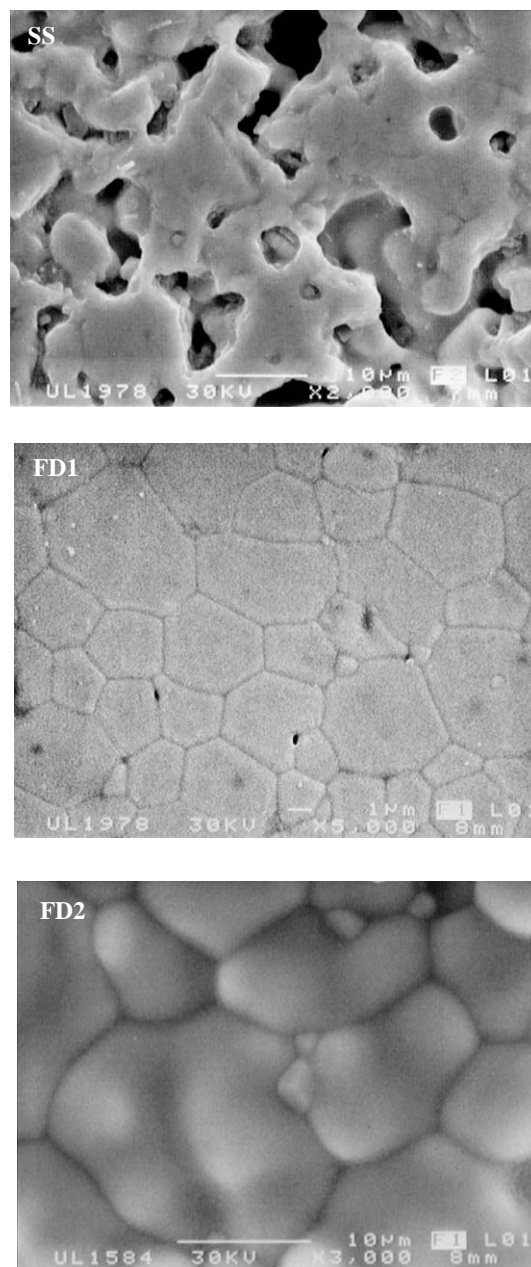

Fig. 3. SEM images of sintered pellet of $La_2Mo_2O_9$ obtained from different synthesis methods. Powders prepared by SS reactions and from freeze-dried powders at 1223 K (FD1) and 1373 K (FD2).

Fig. 2. Shrinkage (open symbol) and shrinkage rate (closed symbol) behavior of $La_2Mo_2O_9$ samples prepared from freeze-dried precursors (circles), and from powders prepared by SS reactions (triangles).

different synthesis routes (powder reaction (SS) and freeze drying (FD1)) at 1223 K, during 5 h. The powder reaction route yields poorly densified samples (about 80%). In this case, it is difficult to distinguish the grain boundaries, and to estimate the corresponding grain sizes. On the contrary, pellets obtained from freeze-dried precursors have a high relative density (>95%) and show a grain distribution in the range of about 1–5 μm.

Different SS and FD pellets were also prepared at higher temperature, between 1223 and 1373 K. The SS samples always comprise large pores, and it was impossible to get samples with density higher than 85%, when powders were used as prepared or were ground in a mortar, as in the case of FD samples. However, FD samples can be densified up to 98% when fired at 1373 K. The effect of crystallite size on the densification of FD pellets was also studied. When the freeze-dried powder is calcined above the shrinkage rate temperature (973 K), the crystallites grow forming agglomerates, finally resulting in pellets with lower density.

This material has also been prepared in other works [33,34] by sol–gel precursors at low temperature; nevertheless, the authors reported density values of 90% at a sintered temperature of 1473 K. This density value is lower than the values obtained by us, using the FD method, even when they use much higher temperature and time for sintering than us.

2.5. Electrical measurements

Pellets with a diameter of 9 mm and thickness 1.5–2 mm were uniaxially compressed at 154 MPa, and sintered in air between 1223 and 1373 K for 5 h. This method was used for both types of samples (FD and SS) to be able to compare the sinterability and electrical properties.

Impedance measurements were performed in air which was cooled from 1123 to 493 K at 5 K min^{-1} (accuracy ±1 K) with a dwell time of 10 min between measurements. Two electrodes of platinum paste were painted on either side of the sample, and fired at 1223 K during 15 min to ensure adhesion, without excessive microstructural changes, compared to the original sintering conditions.

The Solartron 1260 impedance analyzer was used for electrical characterization, including an assessment of grain boundary effects. Spectra were obtained in the frequency range from 0.1 Hz to 1 MHz with an applied voltage of 25 mV in the temperature range of 1123–823 K and 100 mV in the range 773–523 K, which was controlled by the computer program ZPlot. Data analysis was made by equivalent circuits using the program ZView [35] allowing us to estimate the different contributions of the conductivity.

3. Results and discussion

3.1. Structural characterization

The high-temperature β-$La_2Mo_2O_9$ form has a cubic symmetry with space group $P2_13$ (no. 198). However, as mentioned previously, the structure of the α-$La_2Mo_2O_9$ is not yet well established. The last compound was initially reported to crystallize in cubic symmetry with the cell parameter 7.155 Å [25]. But studies using both electron and neutron diffraction have confirmed that α-$La_2Mo_2O_9$ presents lower symmetry than the cubic high-temperature β-form [24].

Fig. 4 shows the diffraction pattern of α-$La_2Mo_2O_9$ at room temperature and β-$La_2Mo_2O_9$ at 923 K prepared
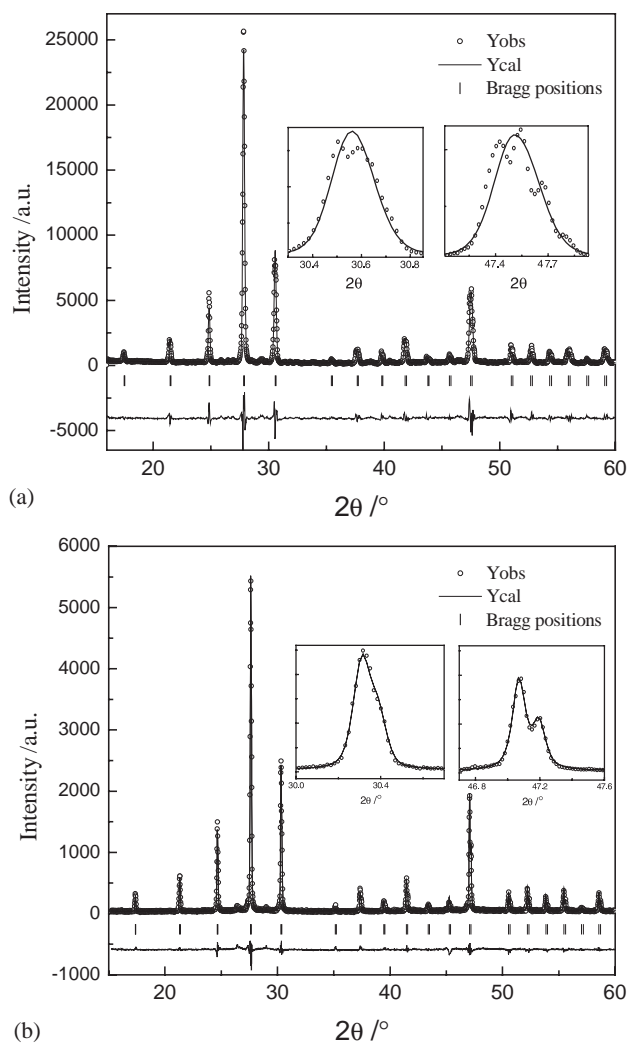
Fig. 4. XRD pattern of (a) α-$La_2Mo_2O_9$ (FD) obtained at room temperature and (b) β-$La_2Mo_2O_9$ obtained at 923 K, showing experimental (circles), calculated (continuous line), and difference profiles. Vertical tics indicate Bragg peaks allowed in the cubic space group $P2_13$. Insets of (a) show some splitting at low temperature, which cannot be fitted in the space group $P2_13$, indicating a distortion of the high-temperature cubic form.

from the freeze-dried precursor and calcined at 1223 K. Though the diffraction patterns have been indexed with the space group $P2_13$ in whole temperature range studied (298–1023 K), some splittings appear in certain Bragg diffraction peaks of the α-$La_2Mo_2O_9$ form as can be observed in the inset of Fig. 4a. These splittings are indicative of the existence of a distortion relative to β-$La_2Mo_2O_9$ [26].

The thermal evolution of the cell volume (per formula unit), recorded on heating process in air and high-vacuum conditions is plotted in Fig. 5 for FD powders and shows a clear deviation for temperatures above 848 K; this can be ascribed to the phase transition from α-$La_2Mo_2O_9$ to β-$La_2Mo_2O_9$. However, a different behavior is clearly observed in air and vacuum atmosphere, in the thermal evolution of cell volume. In air a sharp and discontinuous increase in the cell volume is observed and the change of phase $\alpha \rightarrow \beta$ occurs in an interval of temperature of 20 K. Whereas in vacuum the change in cell volume does not correspond to a sharp increase. The XRD patterns at high temperature in vacuum show that the two phases α and β coexist over a wide temperature range to 1023 K, thus suppressing a discontinuous change in the cell volume. This behavior could be ascribed to a progressive oxygen loss in the reducing conditions provided by the vacuum atmosphere (aproximately 10^{-3} Pa) and it will be studied in a forthcoming paper.

The DSC results shown in Fig. 6 confirm the $\alpha \rightarrow \beta$ phase transition suggested by the temperature dependence of the cell volume. On heating, the onset of the endothermic changes occurs at 842 K and reaches a maximum at about 848 K. On cooling, the onset of the peak is displaced to somewhat lower temperatures (about 833 K). The thermal hysteresis observed
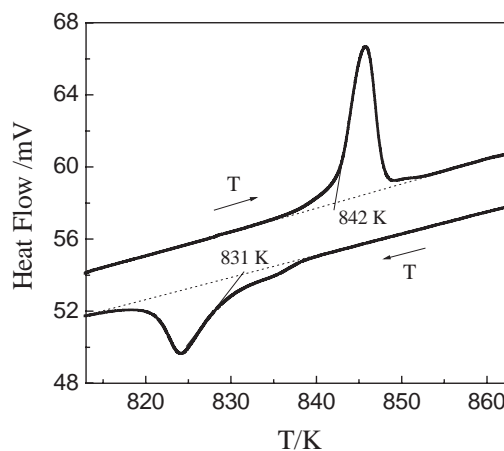
Fig. 6. DSC curves of $La_2Mo_2O_9$ (FD samples) in heating and cooling processes, showing the phase transition of $La_2Mo_2O_9$. A thermal hysteresis of about 11 K is observed.

(around 11 K) is characteristic of a first-order phase transformation.

The changes in thermodynamics parameters enthalpy ($\Delta H \approx 5.5\,kJ\,mol^{-1}$) and entropy ($\Delta S \approx 6.5\,J\,mol^{-1}\,K^{-1}$) at the phase transition were calculated by numerical integration of the recorded DSC thermal curves, after the correction for the calorimetric line base, using the relationships [36]:

$$\Delta H = \int \frac{Q}{v}\,dt \text{ and } \Delta S = \frac{\Delta H}{T_t},$$

where Q is the heat flow (W), v the heating rate ($K\,s^{-1}$), t the time (s) and T_t the transition temperature. Note that the entropy change demonstrates that the low-temperature polymorph is less entropic than the high-temperature form, thus supporting the proposed structural interpretation.

The linear thermal expansion coefficient α can be obtained from the temperature dependence of the unit cell volume (Fig. 5), as described by $v^{-1} \cdot (dv/dT) = 3\alpha$; this was used to obtain the thermal expansion coefficient in the low-temperature range $\alpha_{LT} = 11 \times 10^{-6}\,K^{-1}$ in vacuum and $14 \times 10^{-6}\,K^{-1}$ in air. These values are within in the range expected for other oxygen ion conductors [37]. The thermal expansion coefficient above the phase transition in air is higher than at low temperature $\alpha_{HT} = 18 \times 10^{-6}\,K^{-1}$. The steep slope of the high temperature in vacuum conditions includes a rapid unit cell volume change near the phase transition temperature. Otherwise, this range would yield an unrealistic value of linear thermal expansion coefficient in the order of $40 \times 10^{-6}\,K^{-1}$.

The thermal expansion results shown in Fig. 7 reveal that the phase transformation corresponds to a first-order transition, with a steep volume increase. In this case, the thermal expansion in the high-temperature
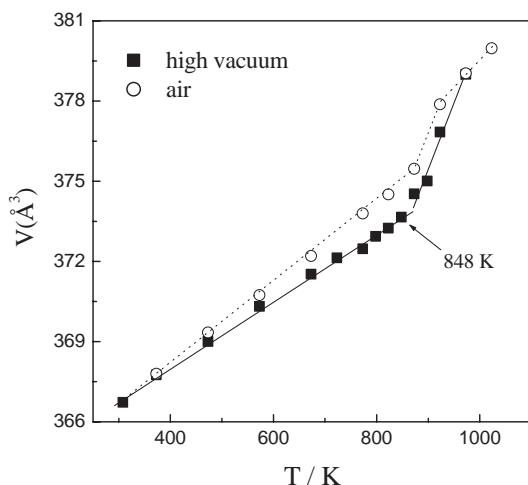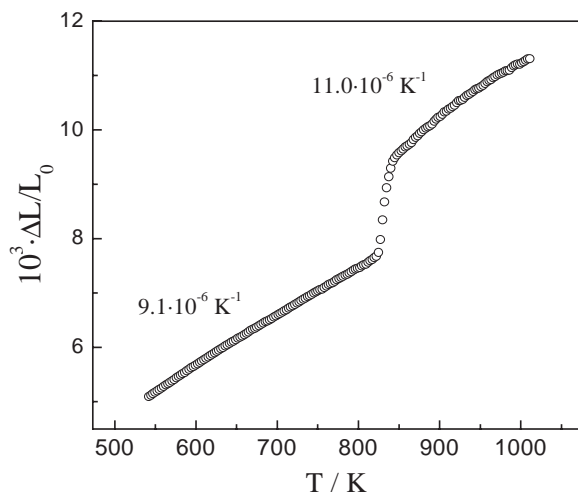
Fig. 5. Thermal evolution of cell volume of $La_2Mo_2O_9$ (FD samples) from XRD data obtained in air (open circles) and high vacuum (closed squares), showing a different behavior in the phase transition $\alpha \rightarrow \beta$ at 848 K.

Fig. 7. Thermal expansion of $La_2Mo_2O_9$ obtained from freeze-dried precursors (FD1) showing the phase transition $\alpha \to \beta$.

range ($\alpha_{HT} = 11.0 \times 10^{-6}\,K^{-1}$) is only slightly higher than in the low-temperature range ($\alpha_{LT} = 9.1 \times 10^{-6}\,K^{-1}$). This value is also somewhat lower than the corresponding value from the dependence of the cell volume.

3.2. Electrical conductivity

The impedance spectra for SS sample sintered at 1223 K and the freeze-dried samples sintered at 1223 (FD1) and 1373 K (FD2) are shown in Fig. 8.

The impedance spectra of SS sample show three different processes. The two processes at high frequency are overlapped and can be ascribed to the bulk (i.e., grain interiors) and internal interfaces (pores and grain boundaries). The third contribution at low frequency is ascribed to the electrode processes. Due to the high porosity of this sample, we did not try to resolve the bulk and grain boundary contributions and only the total conductivity was determined. An additional SS sample sintered at 1373 K was also studied, but it presents similar both density and resistance values and for this reason we do not report it here.

The impedance spectra for FD samples comprises relatively well-separated depressed arcs, which can be described by a series association of $(R_1Q_1), (R_2Q_2)$ and (R_3Q_3) terms, R_i being a resistance contribution, and Q_i a pseudo-capacitance, which is related to the angular relaxation frequency ω_i, and capacitance C_i, as follows $\omega_i = (R_iC_i)^{-1} = (R_iQ_i)^{-1/n_i}$ [38], and thus:

$$C_i = Q_i^{1/n_i}(R_i)^{(1-n_i)/n_i}.$$

The high-frequency contribution possesses typical values of capacitance in the range 20 pF, and was thus ascribed to intrinsic contribution of the grain interiors, and the capacitance of the intermediate frequency
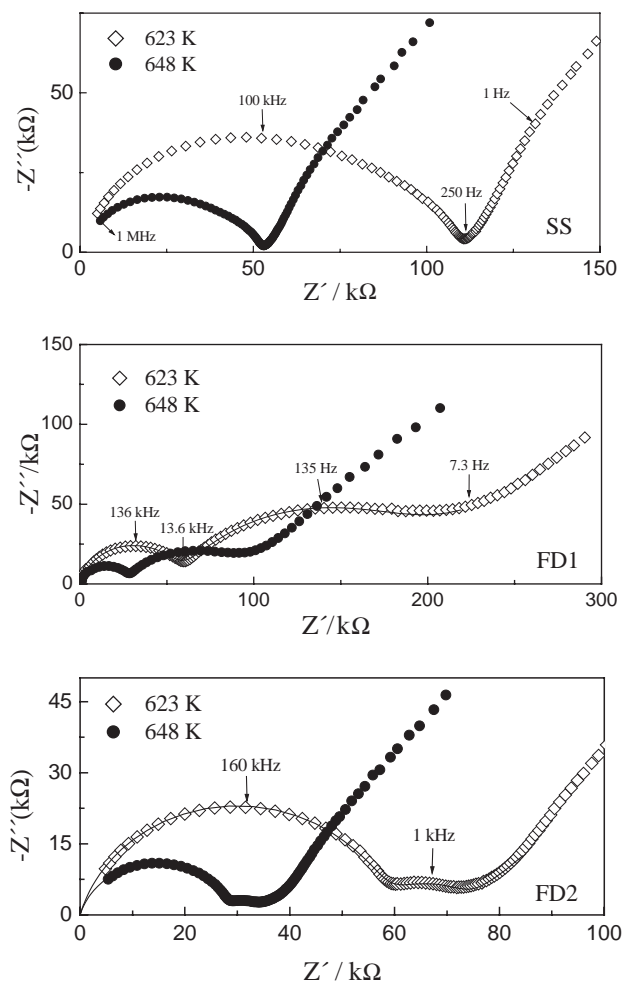

Fig. 8. Impedance spectra of an $La_2Mo_2O_9$ sample obtained from SS reaction and freeze-dried precursor method (FD1 and FD2). The solid line is the fitting result obtained with equivalent circuits.

contribution is the range of 7 nF, which corresponds to internal interfaces (e.g., grain boundaries).

The capacitance of the low-frequency contribution ($>30\,\mu F$) is clearly related to the external material/electrode interface. Some fitting parameters at different temperatures are shown in Table 1.

The dielectric constant of the materials can be estimated from the capacitance of grain interiors, as follows:

$$\varepsilon_r = \frac{LC}{A\varepsilon_0},$$

where ε_0 is the vacuum permittivity, L is the sample thickness (m) and A is the electrode area (m²); this yields a typical value of dielectric constant of about 70. However, this is probably overestimated because the actual equipment has a capacitance detection limit relatively close to the measured values. In these conditions, the cell introduces a spurious capacitance in parallel with the sample, and the actual bulk

capacitance may be overestimated. Nevertheless, this effect is less likely to affect contributions with higher capacitance (e.g., grain boundaries).

The conductivity values, and the corresponding bulk and grain boundary contributions were obtained by taking into account the geometric factor $\sigma = L/(A \cdot R)$, where R is the resistance (Ω) of pellet. The thermal dependence of the conductivity was plotted using Arrhenius equation:

$$\sigma = \frac{\sigma_0}{T}\exp(-E_a/kT).$$

The Arrhenius plot of total conductivity for FD2 (Fig. 9) shows clearly the phase transition at 855 K with a sudden enhancement of the conductivity of about two orders of magnitude in a temperature interval of 20 K. The hysteric behavior is clearly observed during the cooling and heating process and it provides a manifestation of the first-order character of the $\alpha \rightarrow \beta$ phase

transition. The cooling curve displays higher conductivity around the phase transition. This fact indicates the persistence of the high-temperature β-form below the onset of the transition temperature. From the slopes of the Arrhenius plot, the activation energies of the α and β-form were determined. The activation energy below the phase transition 1.15 eV is slightly higher than above the phase transition 1.05 eV.

In Fig. 10, the Arrhenius plots of total conductivity for the different samples prepared are shown. In all the samples the phase transition is observed at the same temperature, although there are differences in the conductivity values. Even though FD1 samples present better microstructure than SS sample, the small grain size obtained (1–5 μm) increases the resistance of grain boundary, obtaining slightly smaller conductivity values when compared to SS. These values of conductivity obtained for FD1 and SS are similar with those previously published [23]. When the sintering temperature is increased to 1373 K for the freeze-dried samples, the grain size increases up to 15 μm, reducing the grain boundary resistance (Fig. 8) and providing higher conductivity than for SS samples. Some conductivity values of the different samples studied are shown in Table 2.

Fig. 11 shows the resistivity values of the bulk (grain interiors), and grain boundaries for FD1, after taking into account the geometric factor (L/A) of the sample. It should be noted that contrary to the bulk resistivity, the y-scale in Fig. 11 is somewhat arbitrary for the grain boundaries, since its geometric factor is far from the one of the pellet and cannot be evaluated. Fig. 11 provides

Table 1
Fitting parameters of *bulk* and grain boundary (gb) processes for freeze-dried sample (FD1) at different temperatures (R=resistance; C=capacitance and; n=exponent of Q_i)

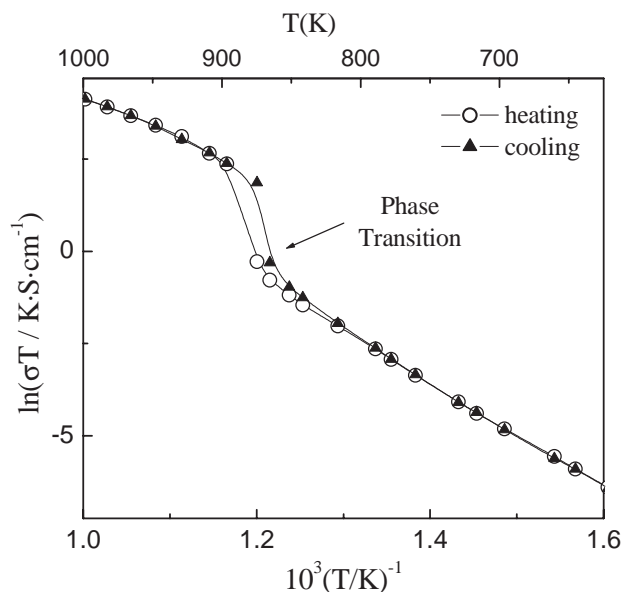| Temperature	623 K	638 K	648 K
R_{bulk} (kΩ)	57.1	36.8	27.0
C_{bulk} (pF)	20.6	19.8	19.6
N_{bulk}	0.84	0.83	0.82
R_{gb} (kΩ)	151.9	91.0	64.7
C_{gb} (nF)	7.20	6.40	8.41
N_{gb}	0.68	0.69	0.70

Fig. 9. Total conductivity of $La_2Mo_2O_9$ obtained from freeze-dried precursors (FD2) showing a first-order phase transition, on heating (open circles) and cooling (filled triangles) processes, with a thermal hysteresis.
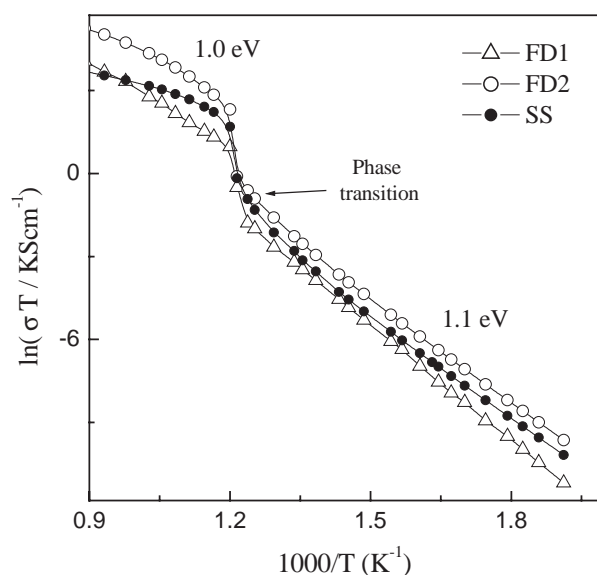

Fig. 10. Arrhenius plots of $La_2Mo_2O_9$ obtained by different synthesis methods: SS reaction sintered at 1223 K, freeze-dried method sintered at 1223 K (FD1) and 1373 K (FD2).

Table 2
Conductivity values obtained for three samples of $La_2Mo_2O_9$ prepared by solid state reaction (SS) at 1123 K, freeze-dried precursor at 1123 K (FD1) and 1373 K (FD2)

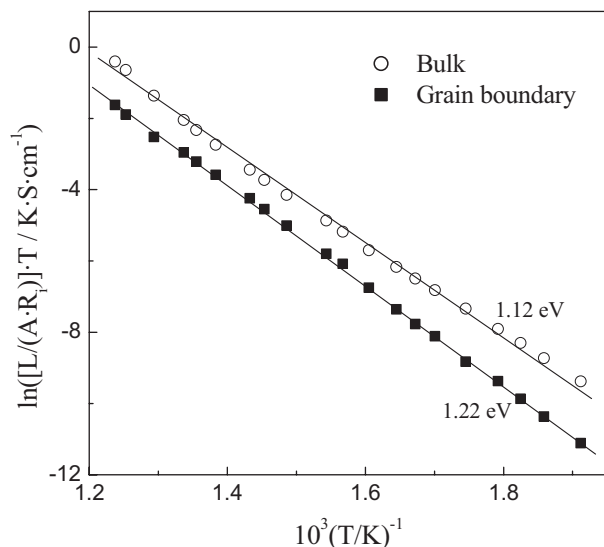| Temperature (K)	Conductivity (S cm^{-1})		
	SS	FD1	FD2
773	1.7×10^{-4}	0.9×10^{-4}	2.6×10^{-4}
873	1.5×10^{-2}	2.0×10^{-2}	2.6×10^{-2}
1073	3.7×10^{-2}	4.0×10^{-2}	14×10^{-2}

Fig. 11. Arrhenius plots of bulk conductivity and the corresponding grain boundary results $L/(R_{gb}A)$ for the freeze-dried sample sintered at 1223 K.

valuable information on activation energy. These results demonstrate the blocking effect of grain boundaries. In addition, the similarity of the values of activation energies 1.12 and 1.22 eV for bulk and grain boundaries, respectively, indicates that the relative role of blocking boundaries is retained with increasing temperatures and further work is needed to improve the microstructures and/or to obtain cleaner and less resistive grain boundaries of this compound.

4. Conclusions

Lanthanum molybdenum oxide, $La_2Mo_2O_9$, has been synthesized using freeze-dried precursor at lower temperature than those used for the ceramic method. The microstructure of sintered pellets is seriously dependent on the synthetic method and the preparation conditions used. Materials prepared from freeze-dried precursors could be sintered up to a relative density of 98%, which is much higher than that of materials prepared by SS

reaction. The thermal, electrical and XRD studies show that the phase transition observed is first-order type.

Electrical conductivities of $La_2Mo_2O_9$ were measured between 523 and 1073 K and the bulk and grain boundary conductivities were studied. The values of activation energy of the bulk and grain boundary conductivities are similar, indicating that the blocking effects of grain boundaries might persist up to relatively high working temperatures. Further work is thus needed to improve the microstructures and suppress those blocking effects of grain boundaries. Moreover, the mechanical stress associated with the large change volume during the phase transition makes pure $La_2Mo_2O_9$ unsuitable for many electrochemical applications.

References

[1] N.Q. Minh, T. Takahashi, Science and Technology of Ceramic Fuel Cell, Elsevier, New. York, 1995.
[2] J.H. Hirschenofer, D.B. Stauffer, R.R. Engelman, M.G. Klett, Fuel Cell Handbook, DOE/FETC-99/1076, 4th Edition, National Technical Information Services, US DOC, Springfield (VA), USA, 1998.
[3] S.C. Singhal, Solid State Ionics 135 (2000) 305–313.
[4] L.J.M.J. Blomen, M.-N. Nugerwa, Fuell Cell System, Plenum Press, New York, 1993.
[5] C.N.R. Rao, J. Gopalakrishnan, New directions in Solids State Chemistry, Cambridge University Press, Cambridge, 1986.
[6] A.J. Moulson, J.M. Herbert, Electroceramics: Materials, Properties and Applications, London, 1989.
[7] J.C. Boivin, G. Mairesse, Chem. Mater. 10 (1998) 2870–2888.
[8] A.M. Azad, S. Larose, S.A. Akbar, J. Mater. Sci. 29 (1994) 4135–4151.
[9] K.R. Kendall, C. Navas, J.K. Thomas, H.C. zur Loye, Chem Mater. 8 (1996) 642–649.
[10] T. Kudo, in: P.J. Gelling, H.J.M. Bouwmeester (Eds.), The CRC Handbook of Solid State Electrochemistry, CRC Press, Boca Ratoon, FL, 1997, p. 195.
[11] J.B. Goodenough, A. Manthiram, P. Paramthaman, Y.S. Zhen, Solid State Ionics 52 (1992) 105–109.
[12] M. Feng, J.B. Goodenough, Eur. J. Solid State Inorg. Chem. 31 (1994) 663.
[13] T. Ishihara, H. Matsuda, Y. Takita, J. Am Chem. Soc. 116 (1994) 3801.
[14] H. Arai, Bull. Ceram. Soc. Japan 27 (1992) 100 (see also Refs. [5,8] and references therein).
[15] H. Inaba, H. Tagawa, Solid State Ionics 83 (1996) 1–16.
[16] K.Q. Huang, M. Feng, J.B. Goodenough, J. Am. Ceram. Soc. 81 (1998) 357.
[17] D.P. Fagg, J.C.C. Abrantes, D. Pérez-Coll, P. Núñez, V.V. Kharton, J.R. Frade, Electrochim. Acta 48 (2003) 1023–1029.

[18] T. Takahashi, H. Iwahara, Y. Nagai, J. Electrochem. Soc. 117 (1970) 244.

[19] F. Abraham, M.F. Debreuille-Gresse, G. Mairesse, G. Nowogrocki, Solid State Ionics 28 (1988) 523–529.

[20] F. Abraham, J.C. Boivin, G. Mairesse, G. Nowogrocki, Solid State Ionics 28–30 (1990) 529–532.

[21] S.A. Kramer, H.L. Tuller, Solid State Ionics 82 (1995) 15–23.

[22] H.L. Tuller, Solid State Ionics 94 (1997) 63–74.

[23] P. Lacorre, F. Goutenoire, O. Bohnke, R. Retoux, Nature 404 (2000) 856–858.

[24] F. Goutenoire, O. Isnard, R. Retoux, P. Lacorre, Chem. Mater. 12 (2000) 2575–2580.

[25] J.P. Fournier, J. Fournier, R. Kohmuller, Bull Soc. Chim. Fr. (1970) 4277–4283.

[26] F. Goutenoire, O. Isnard, E. Suard, O. Bohnke, Y. Laligant, R. Retoux, P. Lacorre, J. Mater. Chem. 11 (2001) 119–124.

[27] X.P. Wang, Q.F. Fang, Solid State Ionics 146 (2002) 185–196.

[28] J.A. Collado, M.A.G. Aranda, A. Cabeza, P. Olivera-Pastor, S. Bruque, J. Solid State Chem. 167 (1) (2002) 80–85.

[29] P. Lacorre, Solid State Sci. 2 (2000) 755–758.

[30] Z.S. Khadasheva, N.U. Venskovskii, M.G. Safronenko, A.V. Mosunov, E.D. Politova, S.S. Yu Stefanovich, Inorg. Mater. 38 (11) (2002) 1168–1171.

[31] J. Rodríguez-Carvajal, FullProf. 98, Laboratoire Léon Brillouin, CEA-Saclay, France, 2000.

[32] T. Roisnel, J. Rodríguez-Carvajal, WinPLOTR, a new tool for powder diffraction, Laboratoire Léon Brillouin-LCSI, France, 2002.

[33] R. Subasri, D. Matusch, H. Näfe, F. Aldinger, J. Eur. Ceram. Soc. 24 (2004) 129–137.

[34] Z.G. Yi, Q.F. Fang, X.P. Wang, G.G. Zhang, Solid State Ionics 160 (2003) 117–124.

[35] ZPlot and Zview. A Software Program for IES Measurements and Analysis, Scribner Associates, NC, USA, 2002.

[36] J.L. McNaugton, C.T. Mortimer, Differential Scanning Calorimetry, Perkin Elmer, Order No. L-604 (reprinted from IRS, Phys. Chem. Ser., Vol. 10, 1–44, Butterworths, London, 1975).

[37] Y. Shiratori, F. Tietz, H.P. Buchkremer, D. Stöver, Solid State Ionics 164 (2003) 27–33.

[38] E. Chinarro, J.R. Jurado, F.M. Figueiredo, J.R. Frade, Solid State Ionics 160 (2003) 161–168.